DE GRUYTER Energy Harvesting and Systems 2015; 2(1-2): 63–71

Special Double Issue Article

Thomas E. Loland, Jaran Sele, Mari-Ann Einarsrud, Per Erik Vullum, Mats Johnsson and Kjell Wiik*

Thermal Conductivity of A-Site Cation-Deficient La-Substituted $SrTiO_3$ Produced by Spark Plasma Sintering

Abstract: During the last decade oxide-based thermoelectric materials have received increased attention due to their high stability and thermal robustness at high temperatures as well as the availability and nontoxic nature of a number of promising candidates. In the present study we are investigating the thermoelectric properties of an n-type La-substituted $SrTiO_3$ with the specific composition $(La_{0.12}Sr_{0.88})_{0.05}TiO_3$. Nanosized powder precursors were spark plasma sintered (SPS) for 5 minutes between 900 and 1,200°C, resulting in densities between 73 and 98% and crystallite sizes between 40 nm and 1 µm. The formation of a rutile phase (TiO_2) was observed in samples sintered at 1,150 and 1,200°C; at lower temperatures only single-phase cubic perovskite was observed. There was no clear evidence that the presence of rutile affected the thermal conductivity (κ). A significant reduction in κ was observed both with increasing porosity and reducing crystallite size, showing a minimum at ~700°C corresponding to ~1.3 W m^{-1} K^{-1}.

Keywords: A-site deficient, La-substituted strontium titanate, nano structuring, n-type, STO, thermal conductivity, thermoelectric oxide

DOI 10.1515/ehs-2014-0042

Introduction

There is an increasing awareness of global warming, a phenomenon basically caused by the ever-increasing utilization of fossil fuels and emission of greenhouse gases such as CO_2. Measures are discussed worldwide as to how to decelerate this unfortunate development and it becomes clear that there is no single solution to this severe problem and that actions must be directed to all greenhouse gas sources aiming at minimizing the emission as much as possible if zero-emission alternatives are unfeasible. Numerous industrial processes (boilers, kilns, ovens, furnaces) as well as various types of transportation all produce ample amounts of waste heat and recovering of this heat to useful energy is one viable route to minimizing greenhouse gas emissions and at the same time improving the economy of any process where recovery is conceivable. According to Valmot (2013) waste heat corresponding to 20 TWh is “produced” by the Norwegian industry annually emphasizing the enormous source of energy.

Thermoelectric (TE) devices offer the opportunity to convert waste heat directly into electricity and represent, due to its simplicity, one of the most promising technologies (Bell 2008). Whether a given material has a potential for TE applications is essentially based on the material’s figure of merit, ZT (Bulusu and Walker 2008):

$$ZT = \frac{S^2 \sigma T}{\kappa} \qquad (1)$$

where S is the Seebeck coefficient (TE power), σ is the electrical conductivity, T is the absolute temperature and κ is the total thermal conductivity corresponding to the sum of electronic and lattice contributions. When ZT increases, the efficiency of energy generation will approach the Carnot limit (Vining 2009), which will be the maximum efficiency allowed by the laws of thermodynamics (White 2008). An average ZT between 1.5 and 2 is considered to enable substantial waste heat harvesting (Bell 2008). Though much of the efforts in TE research so far have

---

***Corresponding author: Kjell Wiik,** Department of Materials Science and Engineering, Norwegian University of Science and Technology, NO-7491 Trondheim, Norway, E-mail: kjell.wiik@ntnu.no
Thomas E. Loland, Jaran Sele: E-mail: jarsele@gmail.com,
Mari-Ann Einarsrud: E-mail: mari-ann.einarsrud@ntnu.no, Department of Materials Science and Engineering, Norwegian University of Science and Technology, NO-7491 Trondheim, Norway
Per Erik Vullum, SINTEF Materials Chemistry, Materials and Nanotechnology, Høgskoleringen 5, Trondheim, Norway, E-mail: PerErik.Vullum@sintef.no
Mats Johnsson, Department of Materials and Environmental Chemistry, Arrhenius Laboratory, Stockholm University, S-106 91 Stockholm, Sweden, E-mail: mats.johnsson@mmk.su.se

focused on primary energy conversion where high *ZT* is desirable, it is also argued that for secondary energy conversion, i.e., recovery of waste heat, TE conversion efficiencies as low as 1% could be economically sustainable provided production costs are low and there is stable long-term performance (Narducci 2011).

Equation [1] gives valuable guidelines with respect to materials selection telling us that we are basically looking for a material with a high TE power and a high electronic conductivity combined with a low thermal conductivity. However, optimizing *ZT* is not straightforward since there are correlations between S, σ and κ: Increasing the TE power will generally lower the electrical conductivity while increasing the electrical conductivity will inevitably increase the electronic contribution to the thermal conductivity. Thus, materials processing and design aimed at increasing *ZT* are demanding due to these contradictions.

A useful first approach is to think in terms of maintaining a sufficiently high electrical conductivity while striving for a low thermal conductivity as possible. This may be feasible due to the fact that phonons possess a certain mean free path and structural units such as grains and precipitates in this range may constrain the propagation of phonons resulting in a significantly reduced thermal conductivity. Generally, the heat flow in a solid material is carried by a spectrum of phonons with widely varying wavelengths and mean free paths typically fluctuating between less than 1 nm to greater than 10 µm (Snyder, Jeffrey, and Toberer 2008). This calls for "phonon scattering agents" at a variety of length scales where the nanoscale, unquestionably, will be the most challenging. Promising results, taking the "nano-perspective," have been reported by a number of research groups (Koumoto et al. 2010).

During the last decade oxide-based TE materials have received increasing attention due to their high stability and thermal robustness at high temperatures as well as the availability and nontoxic nature of a number of promising candidates. It seems to be the consensus in the scientific community that the preferred p-type oxide is the layered $Ca_3Co_4O_9$ composition due to its stability and favorable TE properties in air at temperatures less than 900°C (e.g., Kang et al. 2014).

However, n-type oxide-based materials with sufficient TE properties have since long been challenging. The most promising backbone structures so far are ZnO, $CaMnO_3$ and $SrTiO_3$ (Fergus 2012). There are a large number of investigations related to optimizing the TE properties of $SrTiO_3$ (STO). Both Koumoto et al. (2013) and Walia et al. (2013) give a rather comprehensive review on the state of the art related to STO compositions in particular and oxide TE materials in general. The most common approach is to enhance the electronic conductivity in STO by substitution on A- and/or B-site with a higher valent element (e.g., La^{3+} and Nb^{5+}) and reduce the thermal conductivity by a number of different nanostructuring approaches. The most promising approach, in terms of optimized TE properties, was introduced by Ohta (2007). The concept was based on a two-dimensional electron gas (2DEG) in $SrTiO_3$ realized in $SrTiO_3$/Nb-doped $SrTiO_3$ superlattices and TiO_2/$SrTiO_3$ heterointerfaces, enhancing the Seebeck coefficient by a factor of ~5 compared with bulk STO.

In the present study we will focus on bulk properties of STO materials and take advantage of results published by Shang et al. (2011) who reported high *ZT* values for STO substituted with La on A-site, reaching $ZT = 0.28$ at 773 K for 12% La substitution. Our study is based on the $La_{0.12}Sr_{0.88}TiO_3$ stoichiometry; however, we take this a few steps further by introducing 5% A-site deficiency, $(La_{0.12}Sr_{0.88})_{0.05}TiO_3$, combined with precursor powder produced by spray pyrolysis (nano crystallites) and apply spark plasma sintering (SPS) basically to suppress grain growth and aiming at grains in the nano range. The A-site deficiency is introduced to promote precipitation of secondary phases intended to enhance *ZT* by increased phonon scattering. The precipitation of secondary phases has been reported for similar A-site-deficient La-substituted STO compositions by, e.g., Neagu and Irvine (2010). The variation in thermal conductivity with temperature, density and grain size will be presented and discussed.

Experimental/Methods

Nanosized powder precursors with composition $(La_{0.12}Sr_{0.88})_{0.95}TiO_{3-\delta}$ (referred to as LST) were delivered by Ceramic Powder Technology AS (CerPoTech AS/http://www.cerpotech.com/) produced by spray pyrolysis. The as-received powder precursor was calcined in air at moderate temperature (600°C) and short time (2 hours) to suppress grain growth and subsequently ball milled for 12 hours in 96% ethanol with YSZ grinding balls followed by treatment in a rotavapor (Büchi Rotavapor R-210) to evaporate the ethanol. The powder was finally sieved using a 250 µm sieve. Phase purity was assessed by X-ray diffraction (XRD) and grain size was estimated by both nitrogen adsorption (BET) and XRD (Scherrer), the resulting data are reported in Table 1.

Samples were subsequently prepared by SPS performed under vacuum using a Dr Sinter 2050 SPS (Sumitomo Coal Mining Co., Tokyo, Japan). The inside of the graphite die (20 mm inner diameter) was covered

Table 1: Typical phase purity and representative crystallite size as measured by XRD (Scherrer) and nitrogen adsorption (BET). Particle size estimated from BET was based on $\rho_{\text{theor.LST}} = 5.1595$ g/cm^3. Powder treatment prior to analysis is explained in the text.

Nominal stoichiometry	Crystallite size from XRD, d/(nm)	Crystallite size from nitrogen adsorption (BET)		Phase purity
		Surface area/(m^2/g)	Particle size d/(nm)	
$(La_{0.12}Sr_{0.88})_{0.95}TiO_{3-\delta}$	25	54	22	Traces of $SrCO_3$

with graphite sheets and filled with approx. 5 g LST powder. SPS was performed by applying a constant heating rate of 50°C/min up to the sintering temperature in question, t_{SPS}, where the pressure was manually increased to 50 or 80 MPa and subsequently cooled at >50°C/min (power off, "natural cooling"). Residence time at t_{SPS} for all samples was 5 minutes. Resulting geometry after SPS was typically disc with 20 mm diameter and thickness 3 mm. A summary of the most important SPS process parameters for all samples is given in Table 2.

Table 2: Process parameters and postsintering analysis for all samples sintered by SPS.

t_{SPS} (°C)	Time at t_{SPS} (min)	Applied pressure (MPa)	Postsintering analysis				
			Density	XRD	SEM	TEM	Laser flash
900	5	50	Yes	Yes	–	–	–
925	5	50	Yes	–	–	–	Yes
950	5	50	Yes	Yes	–	Yes	Yes
	5	80	Yes	–	–	–	–
1,000	5	50	Yes	Yes	–	–	Yes
	5	80	Yes	Yes	–	–	Yes
1,050	5	50	Yes	Yes	–	–	Yes
1,100	5	50	Yes	Yes	Yes	–	Yes
1,150	5	50	Yes	Yes	–	–	Yes
1,200	5	50	Yes	Yes	Yes	Yes	–

Density, open and closed porosity were assessed by Archimedes' method using isopropanol and procedure according to ISO 5017:1998. The grain sizes of all sintered samples were estimated by XRD (Bruker D8 Advance DaVinci X-ray diffractometer) based on the solution of the Scherrer equation, which usually gives a fair estimate of grain size normally at $d < 200$ nm. The grain size and crystallite size were assumed equal in these materials. However, strain may also give significant peak broadening and hence give misinterpretations with respect to crystallite size; this issue was further investigated by both Scanning Electron Microscopy (SEM) and Transmission Electron Microscopy (TEM) analysis as described below. The variation in both lattice parameters (Rietveld analysis using Topas 4.2 software) and phase purity with sintering temperature was also determined by XRD analysis. All XRD analyses were performed on mortared samples and are representative for the properties of the bulk phase.

Fracture surfaces of samples sintered at 1,100 and 1,200° C were analyzed by SEM (Zeiss Supra 55 VP) in SE mode giving additional information on both grain size and density.

Samples sintered at 950 and 1,200°C were also prepared for TEM (Jeol ARM200F). The 950°C samples were thoroughly ground in a mortar and transferred to a carbon film used as substrate holder inside the TEM. TEM-bright field images were recorded and analyzed aiming at the assessment of grain/crystallite size. The 1,200°C samples were prepared by tripod wedge polishing before being subjected to TEM analysis and scanning TEM (STEM) images were recorded to reveal both grain size and the presence of secondary phases. The observed secondary phase was carefully examined with respect to chemical composition energy dispersive spectroscopy (EDS) and crystallography (diffraction patterns were recorded at two different tilt angles).

The thermal conductivity was measured by the method of laser flash (Netzsch LFA 457 MicroFlash). The as-received samples from SPS were machined in order to fit into the sample holder of the apparatus (0.5 inch diameter). Machining was done as gentle as possible; however, due to the brittle nature of the samples we were not able to machine samples sintered at 900 and 1,200°C, they all broke into several pieces. Prior to thermal conductivity analysis the samples were coated with graphite to ensure an optimized heat adsorption at the surface. The thermal conductivity was measured between room temperature and 800°C, including three independent measurements for every 100°C. All measurements were conducted in an N_2 atmosphere (flow rate 50 mL/min). The combination of graphite coating and N_2 atmosphere will inevitably give a somewhat reducing atmosphere during the assessment of thermal conductivity. Samples subjected to laser flash apparatus are given in Table 2.

Results and Discussion

Density and Crystallite Size

The density and porosity of the samples are given in Figure 1. The density for samples sintered at 50 MPa varies from less

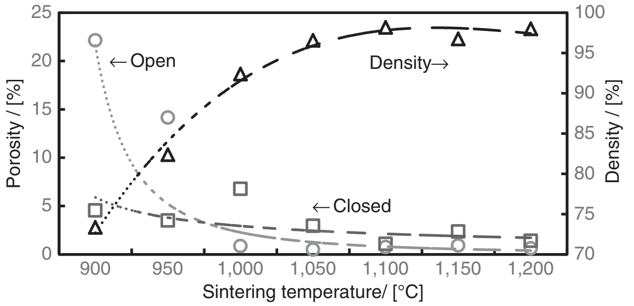

Figure 1: Density and porosity (open and closed) of samples as measured by the Archemedes' method. Samples were sintered for 5 minutes at the given temperature with 50 MPa applied pressure. "Theoretical density," as measured by XRD, was 5.1595 g/cm^3.

than 75% at 900°C and becomes virtually independent of temperature above 1,100°C corresponding to a final density of approx. 98%. According to classic sintering theory the open pores should close at ca. 92% density (German 1996), which is in fair agreement with the results given.

The variation in crystallite size with sintering temperature is presented in Figure 2. However, for crystallite size above 200 nm grain size was estimated from SEM micrograph (Figure 5b) and STEM image (Figure 6b). Based on the images the average grain size at 1,200°C was about 1 µm and is included in Figure 2. At 950°C the grain size according to XRD is less than 50 nm which is in accordance with the grains observed in Figure 6a (TEM bright field image) and indicates that the contribution from strain is insignificant with respect to the assessment of crystallite size in this case.

The ultimate density is reached at about 98% at 1,100°C (Figure 1) and becomes essentially temperature independent above 1,100°C. With reference to Figure 2 it is interesting to notice that the grain growth is significant between 1,100°C (130 nm) and 1,200°C (1 µm), almost increasing with a factor 8 although the density is virtually fixed at 98%. The substantial grain growth combined with a high density is also confirmed in Figure 5, showing tiny grains at the limit of SEM resolution at 1,100°C while the fracture surface at 1,200°C discloses extensive grain growth. Both fracture surfaces confirm a high bulk density, and whereas the fracture mode is difficult to tell at 1,100°C the fracture mode at 1,200°C is essentially trans-granular. These results emphasize the flexibility of the SPS method, being able to produce high density at the same time as the grain size may be varied significantly.

Variation in Lattice Parameter with Sintering Temperature

The lattice parameter against sintering temperature is reported in Figure 3 and is based on Rietveld analysis of XRD data. There is a significant reduction in the cell parameter up to ca. 1,100°C above which it becomes essentially independent of temperature. According to Schmidbauer, Kwasniewski, and Schwarzkopf (2012) the cubic cell parameter for pure $SrTiO_3$ is 3.905 Å, which is indicated by the lower broken line in Figure 3, the upper broken line at 3.9089 Å corresponds to 10% doping with La on A-site as reported by Wang and Wang (2013). Lattice expansion with increasing La substitution is due to the reduction of Ti as described in eq. [2].

$$\mathrm{La_2O_3}{+}2\mathrm{Ti}_{\mathrm{Ti}}^{x}\xrightarrow{\mathrm{SrTiO_3}}2\mathrm{La}_{\mathrm{Sr}}^{\bullet}{+}2\mathrm{O}_{\mathrm{O}}^{x}+\frac{1}{2}\mathrm{O_2}(g)+2\mathrm{Ti'}_{\mathrm{Ti}} \qquad (2)$$

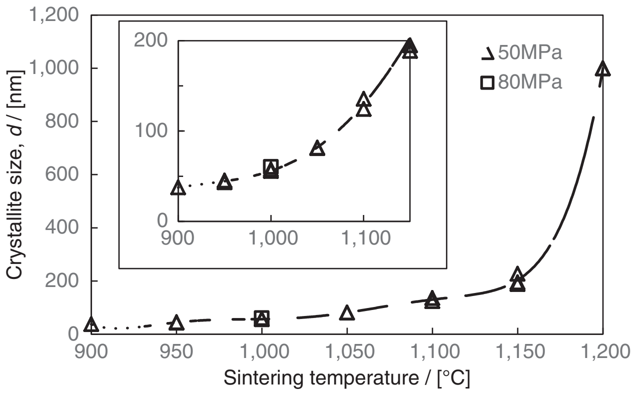

Figure 2: Crystallite size vs. sintering temperature for samples sintered at 50 MPa and 80 MPa, respectively. Size is assessed by XRD between 900 and 1,150°C and estimated from Figure 5b and Figure 6b at 1,200°C. The inset shows a more detailed crystallite size development up to 1,150°C.

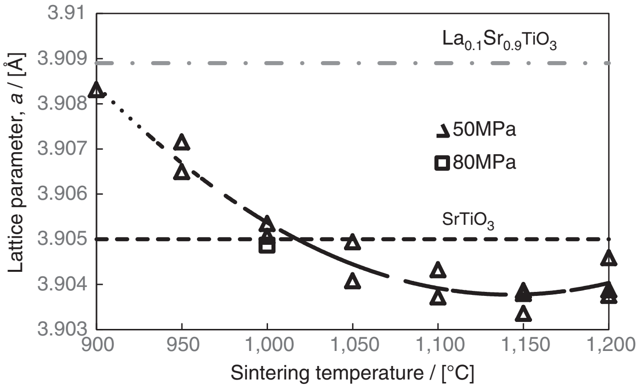

Figure 3: The variation in lattice parameter with sintering temperature for the primary phase based on Rietveld analysis. Lattice parameter for $La_{0.1}Sr_{0.9}TiO_3$ (Wang and Wang 2013) and $SrTiO_3$ (Schmidbauer et al. 2012) is added as horizontal, broken lines.

In our case we have a somewhat higher La substitution level (12%), on the other side the 5% A-site deficiency corresponds to an La substitution level close to 10%. A-site deficiency may be either ionic compensated, viz.,

$$\mathrm{O(nil)} \overset{\mathrm{SrTiO_3}}{\longrightarrow} V_{\mathrm{Sr}}'' + V_{\mathrm{O}}^{\bullet\bullet} \tag{3}$$

or electronic compensated by the formation of $\mathrm{Ti}'_{\mathrm{Ti}}$, the latter would correspond to a lattice expansion. Samples subjected to SPS are in this case exposed to a rather reducing atmosphere, due to the presence of a reducing environment such as graphite felt, thus the extent of Ti reduction is expected to increase with temperature as indicated in eq. [4] followed by lattice expansion.

$$2\mathrm{Ti}_{\mathrm{Ti}}^{x} + \mathrm{O}_{\mathrm{o}}^{x} \rightarrow 2\mathrm{Ti}'_{\mathrm{Ti}} + V_{\mathrm{O}}^{\bullet\bullet} + \frac{1}{2}\mathrm{O_2}(g) \tag{4}$$

The observed lattice contraction with temperature is thus somewhat unexpected. It is evident from the XRD analysis given in Figure 3 that an increasing amount of a secondary TiO_2-rich phase (rutile) is formed with increasing temperature inevitably reducing the A-site deficiency and resulting in a more stoichiometric perovskite. The presence of several phases exhibiting large variations in thermal expansion coefficient (TEC) may during cooling result in remnant strain in the sample followed by a possible shift in the lattice parameters. $SrTiO_3$ phases possess a TEC (de Ligny and Richet, 1996) about a factor 3 larger than the anisotropic TiO_2 (Henderson, Knight, and Lennie 2009). On cooling this should in principle result in a tensile stress in the strontium titanate phase (expanded lattice) and compressive stress (lattice contraction) in the rutile phase, and do not correspond to the observations reported in Figure 3. It should also be noted that XRD analysis did not disclose any strain in the major phase. A small increase in the lattice parameter is observed between 1,150 and 1,200°C, probably due to the formation of the rutile phase which reduces the extent of A-site deficiency. However, a more detailed TEM investigation combined with EDS analysis will be necessary to explain the variation in lattice parameters with temperature.

Phase Relations

An important motivation for investigating an A-site-deficient compound such as $(La_{0.12}Sr_{0.88})_{0.95}TiO_{3\text{-}\delta}$ was the enhanced probability to promote precipitation of secondary phases able to scatter phonons and accordingly reduce the thermal conductivity. Figure 4 shows that a highly crystalline cubic perovskite phase is formed as the major phase while an increasing amount of a secondary TiO_2 phase is formed between 1,150 and 1,200°C; however, it cannot be ruled out that traces of a secondary phase also are present at even lower temperatures (Figure 5). The presence of the TiO_2 phase at 1,200°C is also evident from the STEM image given in Figure 6b–e and confirms that the secondary phase indeed is TiO_2 with a rutile structure. According to Figure 6b TiO_2

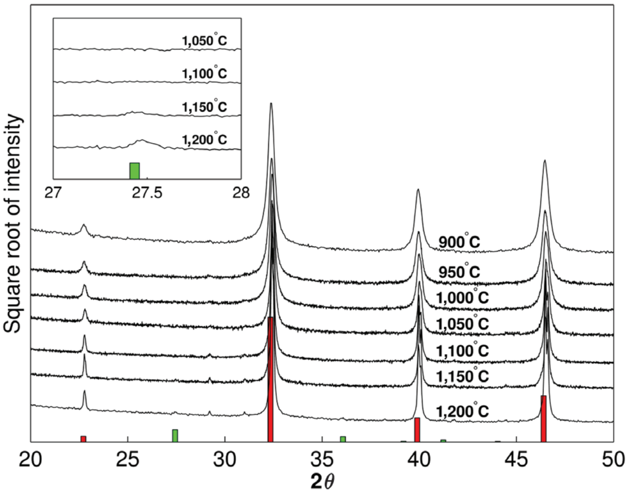

Figure 4: XRD data for samples sintered between 900 and 1,200°C. Red lines represent the main phase (based on PDF 04-002-1010 for $La_{0.1}Sr_{0.9}TiO_3$) while green lines represent the secondary phase (based on PDF 04-003-0648 for TiO_2). The inset shows details for the development of the TiO_2 phase. (The minor peaks at both sides of $2\theta = 30°$ are artifacts due to secondary radiation from W originating from the X-ray tube.)

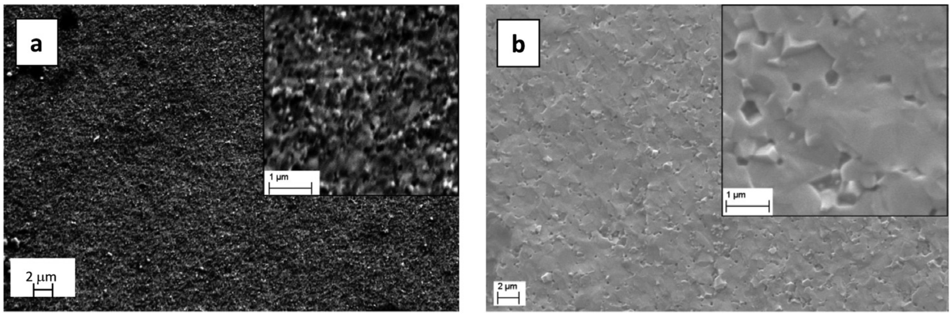

Figure 5: (a) SEM image of fracture surface of sample sintered at 1,100°C and 50 MPa applied pressure. (b) SEM image of fracture surface of sample sintered at 1,200°C and 50 MPa applied pressure.

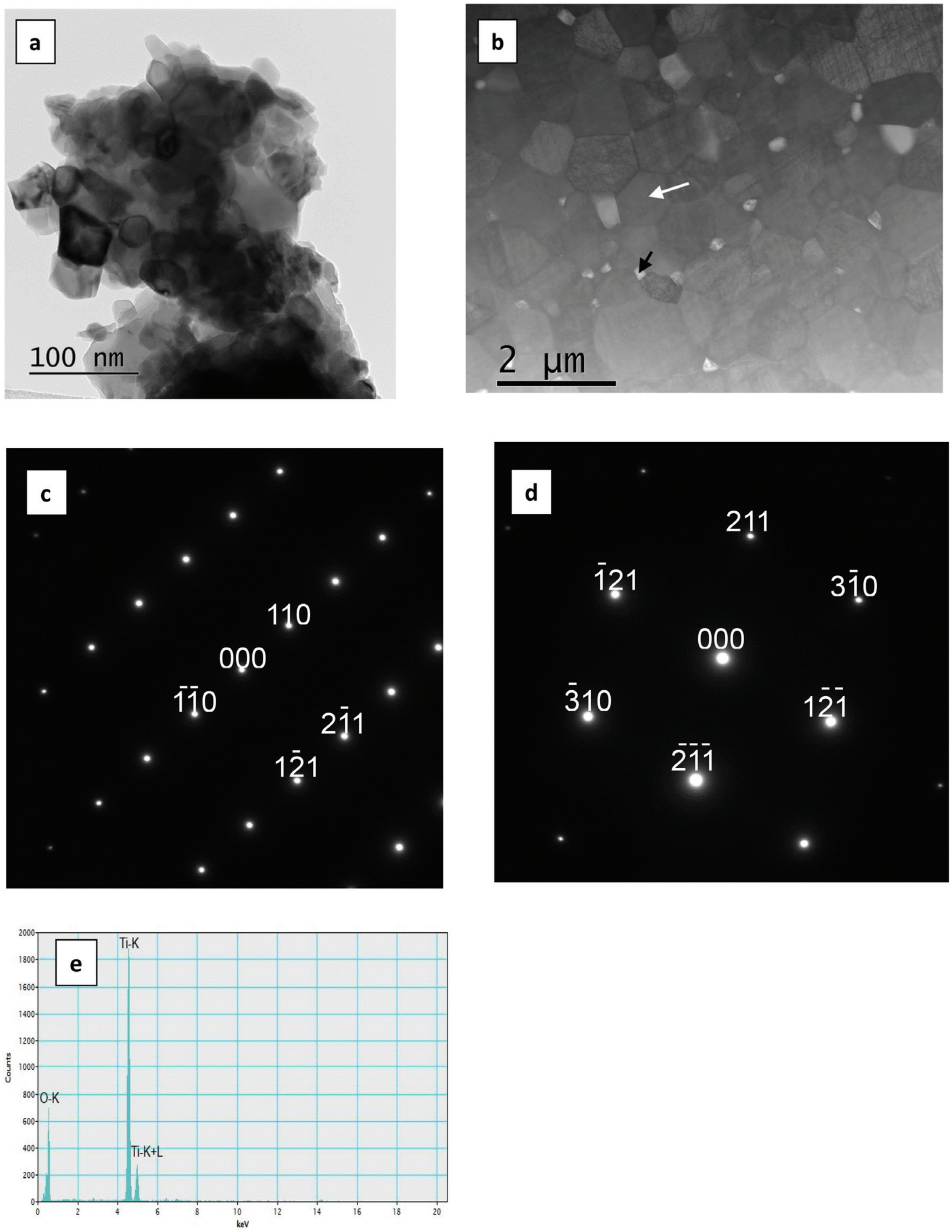

Figure 6: (a) TEM bright field image of sample sintered at 950°C and 50 MPa applied pressure (crushed sample). (b) STEM image of sample sintered at 1,200°C and 50 MPa applied pressure (wedge polished sample). Bright particles are TiO_2 (black arrow), darker particles are primary phase (white arrow). (c)–(d) Diffraction patterns resulting from the secondary phase (bright grain indicated by black arrow in 6b) obtained for two different tilting angles. Indexation is according to rutile (TiO_2). Sample sintered at 1,200°C and 50 MPa applied pressure. (e) EDS analysis of secondary phase (bright grain indicated by black arrow in 6b) in samples sintered at 1,200°C and 50 MPa applied pressure.

seems to form at triple points between grains of the major phase with an average grain size around 200 nm, indicating that nucleation and growth take place at grain boundaries. The transport of Ti ions to the grain boundaries must take place via lattice diffusion in the major phase, and the high activation energy of this type of diffusion explains why it is observed only at the highest sintering temperatures.

Thermal Conductivity

The thermal conductivity is given in Figure 7 for samples sintered at temperatures between 925 and 1,150°C. All samples show a thermal conductivity descending with increasing temperature up to approx. 600°C, consistent with the phonon mean free path, l_{phonon}, being proportional to $1/T$ (Kingery, Bowen, and Uhlmann 1976).

$$l_{\text{phonon}} \propto \frac{1}{T} \tag{5}$$

For samples sintered at the lowest temperatures (925 and 950°C) the thermal conductivity shows a moderate increase at $T > 700$°C, which is attributed to an increasing contribution from heat transfer due to radiation in these relatively porous samples (Figure 1). There is a significant variation in both grain size and porosity between the samples which complicates the immediate interpretation of the results. It is seen that for samples sintered at 1,050°C and below, both porosity and grain size decrease noticeably and the reduction in thermal conductivity may be a combination of both factors.

Wang et al. (2010) were able to model how the thermal conductivity for undoped strontium titanate ($SrTiO_3$) varied with both porosity and grain size. The effect of porosity was estimated by the Klemens model (Schlichting et al. 2001):

$$\kappa_{\text{eff}} = \frac{\kappa}{1 - \frac{4}{3}\varphi} \tag{6}$$

where κ_{eff} is the thermal conductivity of fully dense ceramic and κ is the actual measured thermal conductivity at volume fraction porosity ϕ. This equation may be applied to "remove" the contribution from pores and assess the thermal conductivity of the solid phase. Furthermore, the variation in thermal conductivity, κ, with grain size was estimated from the following equation:

$$\kappa = \frac{\kappa_0}{1 + \frac{\kappa_0 R_K}{d}} \tag{7}$$

where κ_0 is the thermal conductivity of bulk single crystal and R_K is the interfacial thermal resistance due to grain boundaries. $\kappa_0 = 10$ W m^{-1} K^{-1} at 300 K and 4.2 W m^{-1} K^{-1} at 1,000 K, whereas the Kapitza resistance, $R_K = 4.98 \times 10^{-9}$ m^2 K W^{-1} at 300 K and 3.41×10^{-9} m^2 K W^{-1} at 1,000 K. Thus for a given material at a constant temperature the variation in thermal conductivity with grain size may be assessed, given that R_K is independent of grain size. Based on the porosities reported in Figure 1 and grain size given in Figure 2 the variation in thermal conductivity with grain size at various isoporosities is calculated and reported in Figure 8, given that the material is pure,

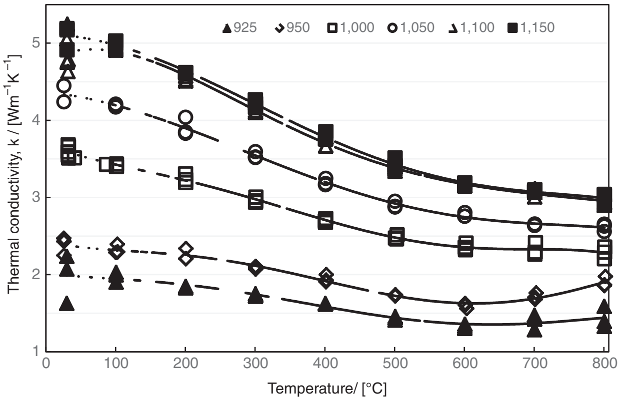

Figure 7: Thermal conductivity measured between room temperature and 800°C for samples sintered between 925 and 1,150°C at 50 MPa.*l*

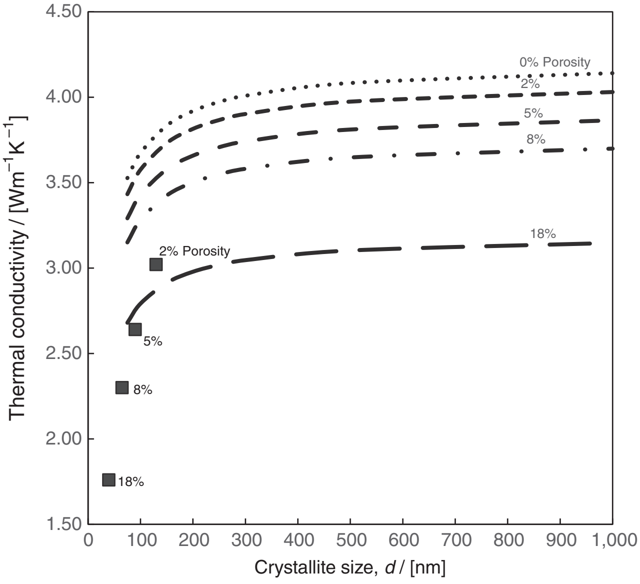

Figure 8: Modeled thermal conductivities for $SrTiO_3$ vs. crystallite size for various isoporosities at 1,000 K. The model is based on Wang et al. (2010). Experimental values from this work for $(La_{0.12}Sr_{0.88})_{0.05}TiO_3$ (filled squares) are included, taken from Figure 7 (numerical values are given in Table 3).

Table 3: Comparing modeled data from Figure 8 ($SrTiO_3$) with experimental data from Figure 7 ($(La_{0.12}Sr_{0.88})_{0.05}TiO_3$.

t_{SPS} (°C)	Density (%)	Porosity (%)	κ_{meas} (W m^{-1} K^{-1})	d (nm)	κ_{mod} (W m^{-1} K^{-1})	$\frac{\kappa_{mod}-\kappa_{meas}}{\kappa_{mod}}$ 100 (%)
950	82	18	1.76	≈40	2.35	25
1,000	92	8	2.30	≈65	3.07	25
1,050	95	5	2.64	≈90	3.38	22
1,100	98	2	3.02	≈130	3.68	18

stoichiometric $SrTiO_3$. Values from own measurements, as reported in Figure 7, are also included and numerical values are given in Table 3. From Figure 8 and Table 3 it is evident that $(La_{0.12}Sr_{0.88})_{0.95}TiO_{3-\delta}$ shows a significant reduction in thermal conductivity compared with estimated values for $SrTiO_3$, with 25% lower values for samples sintered at 950°C, demonstrating that doping with La combined with A-site deficiency effectively reduces thermal conductivity.

The isolated effect of the presence of TiO_2 on the thermal conductivity is not easily deconvoluted. With reference to Figures 4 and 7 the thermal conductivity for samples sintered at 1,100 and 1,150°C, respectively, is similar although TiO_2 is observed at 1,150 but absent at 1,100°C. The density is similar for both samples, and although there is some variation in crystallite size (Figure 2), at least these two samples indicate that the influence of TiO_2 is insignificant with respect to the thermal conductivity.

The significant decrease in thermal conductivity from 1,050 to 925°C coincides with a substantial reduction in both density (Figure 1) and crystallite size (Figure 2). These results correspond well with the behavior described in Figure 8, where it is evident that reducing the crystallite size below 100 nm significantly reduces the thermal conductivity, it is also clear from the same figure that increased porosity has a similar effect. The reduced thermal conductivity in this regime is thus a combination of crystallite size and porosity.

Correlations with Related Investigations

Shang et al. (2011) have also reported thermal conductivity for stoichiometric $La_{0.12}Sr_{0.88}TiO_{3-\delta}$ synthesized by the solid state method and these values are similar to our values for samples sintered at 1,150°C; however, Shang's samples are rather porous (density 85.6%) and the thermal conductivity will undoubtedly increase significantly if sintered to almost full density, as predicted in Figure 8.

Shang et al. (2010) also investigated compositions with lower substitution levels of La, such as $La_{0.08}Sr_{0.92}TiO_3$; these samples were synthesized by a sol–gel route and powders were subjected to SPS at 930°C resulting in a density of 77.8% and an average grain size around 300 nm. The resulting grain size is significantly larger than our samples (<50 nm) sintered at 925°C whereas the porosity is similar. They report, however, a variation in thermal conductivity from 1.8 W m^{-1} K^{-1} at 50°C to 1.2 W m^{-1} K^{-1} at 500°C, values which are comparable to values reported for our samples sintered at 925°C. It should be emphasized that reducing the level of La substitution also corresponds to a reduction in the electronic conductivity (eq. [2]) and accordingly reduce the thermal conductivity due to electrons. This may have affected the values reported by Shang et al.

There are several investigations reporting on the effect of A-site deficiency in STO. Most of these investigations are related to applications such as anode materials in solid oxide fuel cells (SOFCs) and are essentially focusing on the possible enhancement of electronic conductivity and catalytic activity at reducing conditions (Blennow 2006; Neagu and Irvine 2010, 2011; Burnat et al. 2012). One exception is, however, Kovalevsky et al. (2014), who investigated the effect of A-site cation-deficient donor-substituted (Pr and Nb) STO with respect to TE performance. According to XRD analysis all compositions were single phase and they concluded that A-site deficiency enhanced electrical properties but with less effect on the thermal conductivity.

The contribution from electrons with respect to the thermal conductivity has not been treated in the present investigation, due to the lack of electronic conductivity data. However, work is in progress characterizing the electronic conductivity as well as Seebeck coefficient for all materials reported in Figure 7, and these results as well as ZT values will be reported in a subsequent paper.

Conclusions

In the present work we have spark plasma sintered (SPS) nanosized ceramic powders with composition $(La_{0.12}Sr_{0.88})_{0.05}TiO_3$. The sintering temperature was varied from 900 to 1,200°C and resulted in densities in the range from 73 to 98% and crystallite size from 40 nm to 1 μm. The formation of a rutile phase (TiO_2) was observed in samples sintered at 1,150 and 1,200°C, at lower temperatures only single-phase cubic perovskite was observed. The thermal conductivity for samples sintered between 925 and 1,150°C was measured by the method of laser flash from room temperature to 800°C. There was no clear experimental evidence that the presence of the secondary rutile phase suppressed the thermal conductivity.

However, a significant reduction in thermal conductivity with both increasing porosity and reducing crystallite size was evident, showing a minimum thermal conductivity, corresponding to 1.3 W m^{-1} K^{-1} at 700°C, for samples sintered at the lowest temperature (925°C). The variation in thermal conductivity with porosity and crystallite size was in accordance with a simple model based on data given in the literature. The cubic lattice parameter for $(La_{0.12}Sr_{0.88})_{0.05}TiO_3$ showed a clear trend of contraction with increasing sintering temperature, the reason for this behavior was not obvious.

Acknowledgments: Funding provided by the Norwegian Research Council (NFR), Thermoelectric materials: Nanostructuring for improving the energy efficiency of thermoelectric generators and heat pumps (NANO2021/THELMA), project no. 228854, is acknowledged.

References

Bell, L. E. 2008. “Cooling, Heating, Generating Power, and Recovering Waste Heat with Thermoelectric Systems.” *Science* 321: 1457–61.

Blennow, P., et al. 2006. “Effects of Sr/Ti-Ratio in $SrTiO_3$-Based SOFC-Anodes Investigated by the Use of Cone-Shaped Electrodes.” *Electrochimica Acta* 52 (4): 1651–61.

Bulusu, A., and D. Walker. 2008. “Review of Electronic Transport Models for Thermoelectric Materials.” *Superlattices and Microstructures* 44: 1–36.

Burnata, D., A. Heelc, L. Holzera, D. Katab, J. Lisb, and T. Graulea. 2012. “Synthesis and Performance of A-Site Deficient Lanthanum-Doped Strontium Titanate by Nanoparticle Based Spray Pyrolysis.” *Journal of Power Sources* 201 (1): 26–36.

de Ligny, D., and P. Richet. 1996. “High-Temperature Heat Capacity and Thermal Expansion of $SrTiO_3$ and $SrZrO_3$ Perovskites.” *Physical Review B* 53 (6): 3013–22.

Fergus, J. W. 2012. “Oxide Materials for High Temperature Thermoelectric Energy Conversion.” *Journal of the European Ceramic Society* 32: 525–40.

German, R. M. 1996. *Sintering Theory and Practice*, p. 155. New York: John Wiley & Sons, Inc. ISBN 0-471-05786-X.

Henderson, C. M. B., K. S. Knight, and A. R. Lennie. 2009. “Temperature Dependence of Rutile (TiO2) and Geikielite (MgTiO3) Structures Determined Using Neutron Powder Diffraction.” *The Open Mineralogy Journal* 3: 1–11.

Kang, M.-G., K.-H. Cho, J.-S. Kim, S. Nahm, S.-J. Yoon, and C.-Y. Kang. 2014. “Post-Calcination, a Novel Method to Synthesize Cobalt Oxide-Based Thermoelectric Materials.” *Acta Materialia* 73: 251–58.

Kingery, W. D., H. K. Bowen, and D. R. Uhlmann. 1976. *Introduction to Ceramics*. 2nd ed. New York: John Wiley & Sons, Inc. ISBN 0-471-47880-1.

Koumoto, K., R. Funahashi, E. Guilmeau, Y. Miyazaki, A. Weidenkaff, Y. Wang, and C. Wan. 2013. “Thermoelectric Ceramics for Energy Harvesting.” *Journal of the American Ceramic Society* 96 (1): 1–23.

Koumoto, K., Y. Wang, R. Zhang, A. Kosuga, R. Funahashi, K. Koumoto, et al. 2010. “Oxide Thermoelectric Materials: A Nanostructuring Approach.” *Annual Review of Materials Research* 40: 363–94.

Kovalevsky, V., A. A. Yaremchenko, S. Populoh, A. Weidenkaff, and J. R. Frade. 2014. “Effect of A-Site Cation Deficiency on the Thermoelectric Performance of Donor-Substituted Strontium Titanate.” *The Journal of Physical Chemistry C* 118: 4596–606.

Narducci, D. 2011. “Do We Really Need High Thermoelectric Figures of Merit? A Critical Appraisal to the Power Conversion Efficiency of Thermoelectric Materials.” *Applied Physics Letters 99*: 10.

Neagu, D., and J. T. S. Irvine. 2010. “Structure and Properties of $La_{0.4}sr_{0.4}TiO_3$ Ceramics for Use as Anode Materials in Solid Oxide Fuel Cells.” *Chemistry of Materials* 22 (17): 5042–53.

Neagu, D., and J. T. S. Irvine. 2010, 2011. “Enhancing Electronic Conductivity in Strontium Titanates Through Correlated A- and B-Site Doping.” *Chemistry of Materials* 23 (6): 1607–17.

Ohta, H. 2007. “Thermoelectrics Based on Strontium Titanate.” *Materials Today* 10 (10): 44–49.

Schmidbauer, M., A. Kwasniewski, and J. Schwarzkopf. 2012. “High-Precision Absolute Lattice Parameter Determination of $SrTiO_3$, $DyScO_3$ and $NdGaO_3$ Single Crystals.” *Acta Crystallographica* B68: 8–14. ISSN 0108–7681. doi:10.1107/S0108768111046738.

Schlichting, K. W., N. P. Padture, and P. G. Klemens. 2001. “Thermal conductivity of dense and porous yttriastabilized zirconia” *J. Mater. Sci*. 36: 3003–10.

Shang, P.-P., B.-P. Shang, Y. Liu, J.-F. Li, and H.-M. Zhu. 2011. “Preparation and Thermoelectric Properties of La-Doped, $SrTiO_3$ Ceramics.” *Journal of Electronic Materials* 40 (5): 926–31.

Shang, P. P., B. P. Zhang, J. F. Li, and N. Ma. 2010. “Effect of Sintering Temperature on Thermoelectric Properties of La-Doped $SrTiO_3$ Ceramics Prepared by Sol-Gel Process and Spark Plasma Sintering.” *Solid State Sciences* 12: 1341–46.

Snyder, G., G. Jeffrey, and E. S. Toberer. 2008. “Complex Thermoelectric Materials.” *Nature Materials* 7 (2): 105–14.

Valmot, O. R. 2013. “Enormt Potential for Energisparing.” *Teknisk Ukeblad (in Norwegian)* 15: 30–31.

Vining, C. B. 2009. “An Inconvenient Truth About Thermoelectrics.” *Nature Materials* 8: 83–85.

Walia, S., S. Balendhran, H. Nili, S. Zhuiykov, G. Rosengarten, Q. H. Wang, M. Bhaskaran, S. Sriram, M. S. Strano, and K. Kalentar-zadeh. 2013. “Transition Metal Oxides-Thermoelectric Properties.” *Progress in Materials Science* 58: 1443–89.

Wang, Y., K. Fujinami, R. Zhang, C. Wan, N. Wang, Y. Ba, and K. Koumoto. 2010. “Interfacial Thermal Resistance and Thermal Conductivity in Nanograined $SrTiO_3$.” *Applied Physics Express* 3: 031101-1–031101-3, *The Japan Society of Applied Physics*.

Wang, H., and C. Wang. 2013. “Thermoelectric Properties of Yb-Doped $La_{0.1}sr_{0.9}TiO_3$ Ceramics at High Temperature.” *Ceramics International* 39: 931–46.

White, B. 2008. “Energy-Harvesting Devices – Beyond the Battery.” *Nature Nanotechnology* 3: 71–72.